ANNUAL REVIEWS

Annual Review of Nuclear and Particle Science

Determination of the Proton's Weak Charge and Its Constraints on the Standard Model

Roger D. Carlini,[1] Willem T.H. van Oers,[2] Mark L. Pitt,[3] and Gregory R. Smith[1]

[1]Thomas Jefferson National Accelerator Facility, Newport News, Virginia 23606, USA; email: carlini@jlab.org

[2]TRIUMF, Vancouver, British Columbia V6T 2A3, Canada

[3]Department of Physics, Virginia Polytechnic Institute and State University, Blacksburg, Virginia 24061, USA

Annu. Rev. Nucl. Part. Sci. 2019. 69:191–217

First published as a Review in Advance on August 6, 2019

The *Annual Review of Nuclear and Particle Science* is online at nucl.annualreviews.org

https://doi.org/10.1146/annurev-nucl-101918-023633

Keywords

parity-violating electron scattering, asymmetry, weak charge of the proton, vector quark couplings, running of the weak mixing angle, physics beyond the Standard Model

Abstract

This article discusses some of the history of parity-violation experiments that culminated in the Q_{weak} experiment, which provided the first determination of the proton's weak charge Q_W^p. The guiding principles necessary to the success of that experiment are outlined, followed by a brief description of the Q_{weak} experiment. Several consistent methods used to determine Q_W^p from the asymmetry measured in the Q_{weak} experiment are explained in detail. The weak mixing angle $\sin^2\theta_{\text{w}}$ determined from Q_W^p is compared with results from other experiments. A description of the procedure for using the Q_W^p result on the proton to set TeV-scale limits for new parity-violating semileptonic physics beyond the Standard Model (BSM) is presented. By also considering atomic parity-violation results on cesium, the article shows how this result can be generalized to set limits on BSM physics, which couples to any combination of valence quark flavors. Finally, the discovery space available to future weak-charge measurements is explored.

Contents

1. INTRODUCTION

The Standard Model (SM) is the theory that unifies the strong, electromagnetic, and weak interactions. To date, it appears to be in excellent agreement with virtually all applicable experimental observables. With the observation of the Higgs boson at the LHC, the existence of the last particle explicitly predicted within the SM has now been confirmed (1, 2). However, the SM is known to be incomplete and is likely the low-energy approximation of what needs to be a more extensive theoretical framework that accommodates a larger set of physical phenomena. Known limitations of the SM include the inability to predict some key features of particles within the model's framework, the lack of any straightforward means to include gravity, the inability to account for the existence of dark energy (a candidate for the explanation of the observed accelerated expansion of the Universe) or dark matter that is believed to account for most of the mass of the Universe, and issues with the hierarchies of scale related to the Higgs boson. These various limitations, along with the dearth of new particles observed in the post-Higgs era, have left the theoretical door open for physics beyond the Standard Model (BSM) to be observable at the TeV scale. The TeV scale can be selectively probed by precision tests of fundamental symmetries in parity violation (PV), electric dipole moment measurements, $g-2$ (anomalous magnetic moment of the muon) experiments, neutrino scattering, neutrinoless double-β decay, and other accelerator-based experiments (3, 4). These types of measurements provide a means of reaching mass scales not directly accessible at existing high-energy colliders.

1.1. Milestones in Accelerator-Based Parity-Violation Measurements

It has long been known that the contribution of the weak force in particle interactions can be isolated and studied by conducting PV measurements. PV is possible because within the SM only those interactions mediated by the weak force change sign with the helicity of the particles involved. In this section, we try to summarize a few key milestones and do not attempt to be comprehensive or do justice to all the significant technical and scientific accomplishments of the generations of scientists working in this field.

The era of accelerator-based PV measurements had its origin in 1974 at Los Alamos National Laboratory (LANL) with the first precision (10^{-7}) measurement of hadronic PV in proton–proton scattering at 15 MeV, conducted by Potter et al. (5). The measurement was performed at a Tandem Van de Graaff accelerator with a Lamb-shift polarized-ion source employing the initial use of rapid spin reversal (1 kHz) of a 200 nA longitudinally polarized proton beam and phase-locking analog signal–processing electronics to measure the normalized asymmetry A_z in the total cross section for the two spin states. This effort helped motivate a generation of higher-energy polarized-proton measurements at LANL/Los Alamos Meson Physics Facility (LAMPF), TRIUMF, the Paul Scherrer Institut (PSI), Argonne National Laboratory (ANL)/Zero Gradient Synchrotron (ZGS), and other laboratories. These PV programs were, for the most part, able to achieve their scientific goals while pioneering the experimental methodology and achieving a relatively high degree of precision. They observed the weak interaction in complex systems. However, due to their limited kinematics and theoretical interpretability they were not able to search for BSM physics.

The next major leap forward came by applying key methodologies (primarily rapid helicity reversal, phase-locking signal detection, and precise beam-property control) to electron accelerators at MIT-Bates, the Mainz Microtron, SLAC National Accelerator Laboratory, and Thomas Jefferson National Accelerator Facility (JLab)/Continuous Electron Beam Accelerator Facility (CEBAF). This new generation of PV measurements could now benefit from the structureless nature of the electron probe that, for the first time, enabled the interpretation of results in terms of quantities that are precisely predicted by the SM, even with measurement precision significantly lower than that already achieved with proton probes. The seminal electron accelerator PV measurement was the SLAC E122 experiment performed by Prescott et al. (6), which clearly observed the presence of PV in the neutral weak current and was critical for establishing universal acceptance of the electroweak SM.

However, only the most recent generation of completed experiments would, for the first time, probe for evidence of possible BSM physics. These experiments achieved a precision of a few parts per billion in the measurement of the scattering asymmetry. The two major efforts were the SLAC E158 (7) and JLab Q_{weak} experiments (8). Although both efforts were technically successful, neither observed a significant discrepancy between measurement and the corresponding SM prediction.

1.2. Isolating the Weak Charge of the Proton via a Parity-Violation Measurement

The metrics for a PV measurement are not simply precision and accuracy; the observable(s) must also be clearly interpretable with respect to what is predicted by theory. In the case of the measurement of Q_W^p [also denoted $Q_W(p)$], that theory is the SM. Any significant deviation between the measured and predicted value of Q_W^p would indicate BSM physics, whereas agreement would place new and significant constraints on possible SM extensions. The Q_{weak} experiment's determination of Q_W^p was relatively clean with respect to theoretical interpretability, as the experiment's primary analysis technique relied on experimental data, not theoretical calculations, to remove any remnant hadronic backgrounds after already heavy suppression by the kinematics selected for

the measurement (8). In conjunction with existing higher-Q^2 parity-violating electron-scattering (PVES) data, the extraction of Q_W^p and the weak neutral-current vector-coupling constants C_{1q} is straightforward, allowing the evaluation of possible scenarios of BSM physics.

The experimentally observed quantity is the asymmetry A_{ep} in the elastic scattering cross section of longitudinally polarized electrons (with helicity ± 1) from an unpolarized-proton target:

$$A_{ep} = \frac{\sigma_+ - \sigma_-}{\sigma_+ + \sigma_-}. \quad 1.$$

When expressed in terms of Sachs electromagnetic (EM) form factors G_E^γ and G_M^γ, weak neutral form factors G_E^Z and G_M^Z, and the neutral weak axial form factor G_A, this asymmetry has the form

$$A_{ep} = \left[\frac{-G_F Q^2}{4\pi\alpha\sqrt{2}}\right]\left[\frac{\varepsilon G_E^\gamma G_E^Z + \tau G_M^\gamma G_M^Z - (1 - 4\sin^2\theta_W)\varepsilon' G_M^\gamma G_A^Z}{\varepsilon (G_E^\gamma)^2 + \tau (G_M^\gamma)^2}\right], \quad 2.$$

where

$$\varepsilon = \frac{1}{1 + 2(1+\tau)\tan^2(\theta/2)}, \quad \varepsilon' = \sqrt{\tau(1+\tau)(1-\varepsilon^2)} \quad 3.$$

are kinematical quantities, Q^2 is the four-momentum transfer, $\tau = Q^2/4M^2$ (M is the proton mass), G_F is the Fermi coupling constant, α is the fine-structure constant, and θ is the laboratory electron-scattering angle. For forward-angle scattering, where $\theta \to 0$, $\epsilon \to 1$, and $\tau \ll 1$, the asymmetry can be written as

$$A_{ep} = A_0\left[Q_W^p + Q^2 B(Q^2,\theta)\right], \quad \text{where } A_0 = \left[\frac{-G_F Q^2}{4\pi\alpha\sqrt{2}}\right]. \quad 4.$$

The first term, proportional to Q^2, corresponds to a point-like proton. The second term, $B(Q^2,\theta)$, proportional to Q^4, is the leading term in the nucleon structure defined in terms of neutron and proton EM and weak form factors. Although the nucleon structure contributions in $B(Q^2,\theta)$ can be suppressed by employing lower momentum transfer Q^2, this also has the consequence of reducing the measurement's asymmetry, making (for example) the control of helicity-correlated beam properties relatively more important. Therefore, these trade-offs were investigated as part of the optimization of the experiment. Fortunately, the numerical value of $B(Q^2,\theta)$ can be determined accurately through extrapolation from existing PVES data at higher Q^2. After the available choices for the primary beam energy, scattering kinematics, and practical topologies for the apparatus/detector are folded in, the optimum Q^2, beam energy, and central electron-scattering angle to perform the Q_W^p measurement were determined to be 0.0248 (GeV/c)^2, 1.16 GeV, and $\theta = 7.9^\circ$ in the laboratory frame, respectively.

2. THE EXPERIMENT

The Q_{weak} experiment was an integrating measurement (versus counting events one at a time), meaning that, except for Q^2 acceptance studies at very low beam currents, the ability to apply traditional data cuts and corrections post data collection was somewhat limited. Therefore, the data collected had to be of very high quality upfront. This is the price all integrating measurements must pay in order to achieve the necessary ultrahigh statistical precision. Performing a PV experiment with enough accuracy to be a meaningful test for BSM physics requires measuring the scattering asymmetry at appropriate kinematics (as discussed above), which means balancing the requirement to obtain good counting statistics with the requirement to maintain sufficient

control of the instrumental and background systematics. These considerations impose significant design constraints on beam properties, experimental acceptance, spectrometer design, and all the experimental subsystems that measure systematic effects.

2.1. Methodology and Optimization

The measurement was performed by comparing the scattering rate for the two opposite longitudinal helicity states of the electron beam. Ideally, no property of the apparatus or beam is changed when the longitudinal helicity of the electron beam is reversed, as such changes can give rise to false asymmetries that contaminate the measurement of the physics asymmetry. In practice, such changes always exist to some degree. So, in addition to simply measuring them in order to correct any residual nonzero false asymmetries, experiments must be designed to be as insensitive as possible to these effects. Identifying these contributions and suppressing them are dealt with in part by having multiple helicity reversals on a variety of timescales. The minimization of such false-asymmetry effects is also aided by passive measures such as complete isolation of the helicity signal from the rest of the apparatus and symmetric-apparatus design, as well as active measures such as feedback systems to minimize the amount by which beam properties can change under helicity reversal. Finally, any remaining nonzero sources of false asymmetry need specialized instrumentation designed to measure and correct for them to the precision required by the scientific goals of the measurement.

The eight-sector toroidal magnetic spectrometer concept was selected to increase acceptance to 49% of 2π in ϕ, separate elastic from inelastic events, and provide an intrinsic suppression of the net effect of scattering asymmetries from the small residual transverse polarization (several percent) in the otherwise longitudinally polarized electron beam. The kinematics resulting from using a 1.16 GeV beam and 7.9° scattering permitted a nearly ideal mechanical placement of the magnet and detector system, which, among other attributes, allowed heavy line-of-sight shielding between the detectors and the target/beamline, including a shutter system to selectively block an octant of the collimator system when conducting detector background studies.

Maximizing the figure of merit (FOM) to achieve parts-per-billion-level precision was essential. The FOM is the inverse of the fractional statistical error on Q_W^p squared. Although a useful metric, it is not a measure of the difficulty of the experiment, which would have to consider systematic errors as well. For a fixed running time,

$$\mathrm{FOM} = \frac{A_{ep}^2 P^2 R}{\left(1 + \frac{Q_0^2 B(Q_0^2,\theta_0)}{Q_W^p}\right)^2}, \qquad 5.$$

where A_{ep} is the physics asymmetry, P is the beam polarization, R is the total elastic scattering rate, and Q_0^2 and θ_0 are the central kinematics values. The term in the denominator reflects the fact that it is only the first term in the asymmetry (Equation 4) that is sensitive to Q_W^p, so the FOM is increased by reducing the contribution of the second term that represents the hadronic structure.

The instrumentation of key signals (the primary detector and beam-current monitor systems) with ultralow-noise analog and digital electronics is necessary in order to allow the experimental apparatus to operate as closely as possible to counting statistics near the helicity-reversal frequency. This minimizes the running time necessary to achieve the desired precision. Similar care is necessary in the cryogenic target design to minimize the noise contribution due to density variations (boiling). The incorporation of redundancy in key instrumentation allows important cross-check capability and resiliency during data analysis, including multiple methods/devices for

measurement of beam polarization, beam current, beam position, helicity-correlated beam asymmetries (HCBAs), backgrounds, and so forth. Separating the measurement into multiple running periods allows time to make technical improvements if necessary and to compare results under different conditions. It is prudent to remember that seeking unprecedented precision inevitably brings surprises. Therefore, the use of ancillary detectors to handle unexpected backgrounds can often provide critical insight during data analysis. Last but not least, blinded data analysis is employed to suppress experimenter bias.

2.2. Technical Implementation

Figure 1 shows the essential subsystems of the Q_{weak} experiment (described in detail in Reference 9). The measurement was performed with an electron beam of 180 μA at 1.16 GeV with an average polarization of 89%, which was incident on a 0.344-m-long 20 K liquid-hydrogen target contained in an aluminum cell with thin entrance and exit windows. A set of three precisely made lead collimators defined the scattering-angle acceptance to the range $5.8^\circ < \theta < 11.6^\circ$, with an azimuthal angle coverage of 49% of 2π. The scattered particles entered the eight open sections of a toroidal resistive magnet located between the target and the detectors. This spectrometer separated the elastically scattered electrons from backgrounds consisting of inelastically scattered particles, Møller electrons, and neutral particles. The toroidal spectrometer was azimuthally symmetric around the incident-beam axis in order to negate the first-order effects of helicity-correlated beam-parameter imperfections and residual transverse beam polarizations on the measured asymmetries.

As noted above, the high rates encountered (∼0.9 GHz per detector) required a current-mode readout, in which the photomultiplier tube (PMT) anode current was converted to a voltage that was integrated and digitized 960 times per second. PMTs (with swappable low- and high-gain bases) were employed instead of vacuum photodiodes in order to allow periodic pulse-counting experiments to be performed for acceptance-weighted energy-distribution determinations at incident electron-beam currents of 0.1 nA to 200 nA with drift chambers placed before and after the toroidal magnetic spectrometer. An ancillary symmetric array of four small luminosity monitors was placed on the upstream face of the defining middle collimator. This array allowed monitoring of residual backgrounds from the tungsten/copper beam collimator, which shielded the downstream region from small-angle-scattered particles. Residual diffuse background was monitored by background detectors in the main detector shield bunker.

The GaAs polarized source of electrons and the injector to CEBAF delivered 180 μA of longitudinally polarized electrons to the recirculating linear accelerator, but also delivered intensities of less than 1 nA for control, background, and acceptance measurements. The helicity of the polarized-electron beam was arranged in a pseudorandom sequence of helicity quartets of $(+--+)$ or $(-++-)$ 240 times per second, phase locked with the data readout. This rapid spin reversal also suppressed the noise component due to fluctuations in the cryogenic liquid-hydrogen target density as well as variations in the parameters of the accelerated electron beam. A photographic analogy would be a frame rate high enough that the scene changes only a minuscule amount from image to image. In addition to the rapid spin reversal, two independent methods on a slower timescale of the electron-beam helicity were used to observe/cancel possible false asymmetries. The first one was introduced every 8 h by changing the helicity of the laser beam impinging on the GaAs by insertion of a half wave plate in its path. The second one was introduced monthly by changing the helicity of the electron beam in the injector section with a double-Wien spin rotator. In addition, by calculating an out-of-phase combination of the various slow helicity reversals, it was possible to construct a null version of the scattering asymmetry, which should be

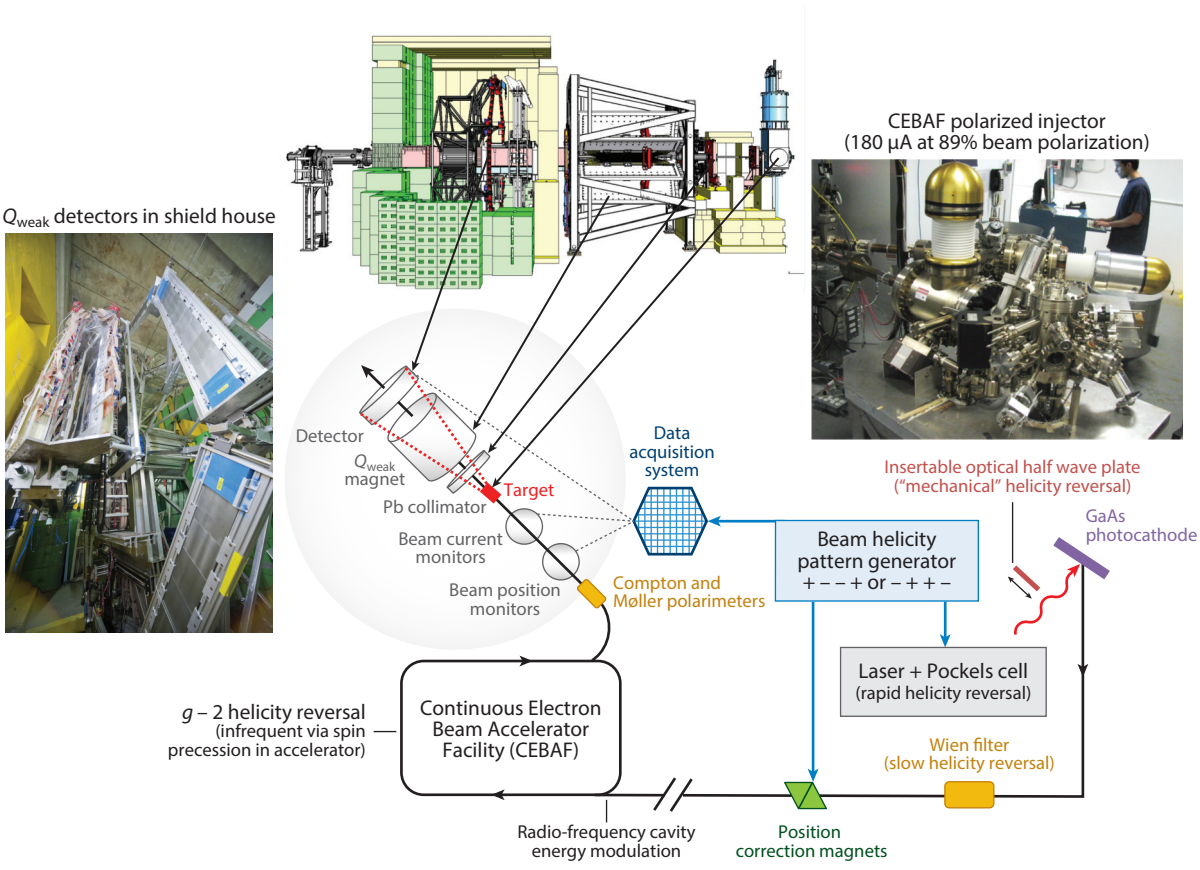

Figure 1

The key subsystems of the Q_{weak} experiment include an ultrastable superconducting accelerator (CEBAF) at JLab, a GaAs polarized source for intense electron beams, a rapid pseudorandom spin-reversal capability to permit the measurements to cleanly isolate the signature of the weak interaction, the periodic insertion of a half wave optical plate into the laser drive of the GaAs source to reverse the electron-beam helicity via a mechanical rather than electrical technique, periodic Wien filter and $g - 2$ spin reversals during data taking to suppress slow helicity-correlated systematic effects, instrumentation to measure/control undesirable helicity-correlated changes in the electron-beam parameters, a 0.34-m-long liquid-hydrogen target, a toroidal magnetic spectrometer to select elastically scattered electrons, an azimuthally symmetric quartz Cherenkov detector system with custom-built electronics employing ultralow-noise electronics, and interchangeable photomultiplier tube bases to permit use with traditional drift chambers during low-luminosity calibration studies. Portions of figure adapted from Reference 8.

zero. It was measured and indeed found to be consistent with zero, implying that all consequential helicity-correlated systematic effects had been accounted for.

Helicity-correlated changes in the accelerated-beam parameters (intensity, position, angle, size, and energy) may lead to false contributions to the measured asymmetries. The effects of helicity-correlated changes in the beam parameters were suppressed by careful tuning of the helicity-defining optics and by active feedback systems in the polarized-injector laser system and beam transport line. A series of beam monitors upstream of the experimental apparatus provided continuous, noninvasive measurement of the beam intensity, position, angle, and energy. The response of the experimental apparatus to fluctuations in the beam parameters was measured in a periodic manner through a beam-modulation system that introduced controlled variations in the

beam position, angle, and size using various magnets along the beam transport line, and similarly in the beam energy using a radio-frequency accelerating cavity. It was also possible to measure these responses using the random natural beam motion, but without the ability to separate the effects on beam parameters one at a time.

2.3. Determination of A_{ep}

In this section, we summarize how the PV elastic electron–proton asymmetry was obtained in the Q_{weak} experiment. Full details of the data analysis that led to that result are presented in Reference 8.

In the Q_{weak} experiment, the basic measurement consisted of averaging the 16 integrated Cherenkov light signals from both PMTs on each of the eight main detectors, and then digitizing these values for each helicity state (approximately every millisecond). These values were normalized to the beam charge. The charge-normalized yields ($Y_{\pm}$) from each helicity quartet formed the raw asymmetry

$$A_{\text{raw}} = \frac{Y_+ - Y_-}{Y_+ + Y_-}. \quad 6.$$

Approximately 1.3 billion such quartets were collected over the course of one calendar year of running. The resulting average raw asymmetry was corrected for a variety of effects that could cause false asymmetries:

$$A_{\text{msr}} = A_{\text{raw}} + A_T + A_L + A_{\text{BCM}} + A_{\text{BB}} + A_{\text{beam}} + A_{\text{bias}}. \quad 7.$$

Here, corrections were made for transverse asymmetry (A_T), detector-signal linearity (A_L), beam-current monitors (A_{BCM}), beamline-background asymmetry (A_{BB}), helicity-correlated beam properties (A_{beam}), and a rescattering bias (A_{bias}). The measured asymmetry (A_{msr}) was then corrected for additional effects to obtain the fully corrected PV elastic electron–proton asymmetry:

$$A_{ep} = R_{\text{tot}} \frac{A_{\text{msr}}/P - \sum_{i=1,3,4} f_i A_i}{1 - \sum_{i=1}^{4} f_i}. \quad 8.$$

The corrections here are for incomplete beam polarization (P), finite acceptance and (EM) radiative corrections (R_{tot}), and the signal dilutions (f_i) and asymmetries (A_i) associated with background processes. **Table 1** summarizes the main contributions to the uncertainty for A_{ep}. The statistical uncertainty dominated, with the main contributions to the systematic uncertainty coming from the following:

- Rescattering bias (A_{bias}). Rescattering of the partially transversely polarized scattered electrons in the lead preradiators of the main detector led to a helicity-dependent light profile along the quartz bars. This effect was not anticipated prior to the experiment, but the symmetric readout of the quartz bars with PMTs at each end and the excellent uniformity of the quartz bars ultimately made this a small effect (10).
- Beam-current monitor correction (A_{BCM}). The beam current was measured noninvasively with radio-frequency-resonant cavities. The observed variation in several such cavities determined the systematic uncertainty.
- Target-windows correction (A_{b1}). The thin (0.1-mm) entrance and exit windows of the hydrogen target cell were made of aluminum 7075 alloy, which contributed ~2.5% to the signal. The asymmetry in scattering from this alloy was measured in dedicated runs with a thick solid target made of the same material as the windows (11–13).

Table 1 Uncertainty contributions to A_{ep}

Contribution	Uncertainty (ppb)
Statistical	7.3
Systematic	
Rescattering bias (A_{bias})	3.4
Beam-current monitor normalization (A_{BCM})	2.6
Target windows (A_{b1})	1.9
Beamline background (A_{BB})	1.4
Beam asymmetries (A_{beam})	1.3
Kinematics (R_{Q^2})	1.3
Beam polarization (P)	1.2
Total of 11 others	2.3
Total systematic	5.8
Total	9.3

- Beamline-background asymmetry correction (A_{BB}). A small contribution (∼0.19%) to the detector signal came from scattered electrons interacting in the beamline and tungsten/copper beam collimator. These events carried a large asymmetry. This effect was not anticipated prior to the experiment, but auxiliary detectors had been installed for such unanticipated false asymmetries. These detectors permitted characterization of this asymmetry so that a correction could be made (14).
- Helicity-correlated beam-property correction (A_{beam}). Residual nonvanishing helicity correlations in the properties of the electron beam were measured and corrected through detector responses determined using a beam-modulation system (15).
- Kinematics (R_{Q^2}). The central Q^2 for the experiment was determined from simulation (16) and benchmarked with measurements from a tracking system that operated in counting mode during special low-beam-current runs.
- Longitudinal beam polarization (P). Beam polarization was measured redundantly with a Compton polarimeter (18) that operated continuously during the run and a Møller polarimeter (17) that operated invasively at low (∼2 μA) beam currents.

The final result for the fully corrected asymmetry was $A_{ep} = -226.5 \pm 7.3(\text{stat.}) \pm 5.8(\text{syst.})$ ppb. This value was determined at an acceptance-averaged Q^2, scattering angle, and incident electron energy of $\langle Q^2 \rangle = 0.0248$ (GeV/c)^2, $\langle \theta \rangle = 7.90^\circ$, and $\langle E_0 \rangle = 1.149$ GeV, respectively.

3. EXTRACTION OF THE WEAK CHARGE AND VECTOR QUARK COUPLINGS

Several methods have been explored to extract the weak charge of the proton Q_W^p from measurements of the PV asymmetries in $\vec{e}p$, $\vec{e}d$, and $\vec{e}$ ^{4}He elastic scattering. These measurements define the PVES database and are loosely grouped into experiments performed by the SAMPLE (19, 20), PVA4 (21–24), G0 (25, 26), HAPPEX (27–31), and Qweak Collaborations (8, 32). The primary method used to extract Q_W^p is described in Reference 32, which presents the commissioning result of the Q_{weak} experiment, constituting approximately 4% of the total data acquired. The final results of the complete Q_{weak} experiment were published in 2018 (8) and constitute the best information currently available on the proton's weak charge. That result also

provided the most precise measure of $\sin^2\theta_w$ below the Z pole, as discussed in Section 4, and the best mass limit associated with PV semileptonic (SL) BSM physics, as discussed in Section 5. Results from several methods used to determine Q_W^p from the Q_{weak} experiment's asymmetry with and without the other asymmetries in the PVES database are also presented in Reference 8. Here, we describe those methods in detail, along with the results that came from them, and then introduce a new and simpler method that is consistent with the results obtained from the other methods.

In the primary method described in References 8 and 32, the weak vector quark couplings C_{1u} and C_{1d}, the strength of the strange form factors $G_{E,M}^s$, and the isovector axial form factor $G_A^{Z(T=1)}$ were varied in a fit of the PVES asymmetries up to $Q^2 = 0.63$ GeV^2. The proton's weak charge was obtained by extrapolating that fit to $Q^2 = 0$. This method is preferred because it is data driven: The measured asymmetries in the PVES database were used to pin down the hadronic structure contributions [$G_{E,M}^s$ and $G_A^{Z(T=1)}$] in order to determine Q_W^p . In this as well as the other methods described below to determine Q_W^p from PVES asymmetries, the dominant contribution to the hadronic structure comes from the relatively well-known EM form factors $G_{E,M}$ from Reference 33.

Alternatively, the hadronic structure contributions can be calculated instead of determined from data in the fit described above (8). This is necessary when using the Q_{weak} datum alone to determine Q_W^p. At the low Q^2 of the Q_{weak} experiment, the contributions from $G_{E,M}^s$ and G_A^Z to Q_W^p are small ($\sim$2%). But it is also interesting and informative to use this technique (calculating $G_{E,M}^s$ and G_A^Z) in a straight-line fit to each Q_W^p determined at the respective Q^2 of each asymmetry measured in the PVES database. In that case, the best fit is (linear and) nearly constant, since to the extent that we know $G_{E,M}^s$ and G_Z, Q_W^p should be the same number independent of Q^2. This new method also helps expose a slight tension between the fit and the calculated strange form factors at higher Q^2.

In the following subsections, we explain how each of these methods is implemented and examine the consistency of the results obtained for Q_W^p. **Figure 2** compares these results with one another and with the SM.

3.1. The Global Fit of the Parity-Violating Electron-Scattering Database

The starting point for relating the PV asymmetry measured in the Q_{weak} experiment to the weak charge of the proton Q_W^p is the tree-level (one-boson exchange) formula in Equation 2. In that equation, the proton's weak neutral form factor $G_{E,M}^{pZ}$ can be expressed in terms of proton, neutron, and strange quark EM form factors by making use of isospin symmetry:

$$G_{E,M}^{p/n,i} = e^{i,u} G_{E,M}^{u/d} + e^{i,d}(G_{E,M}^{d/u} + G_{E,M}^s). \quad 9.$$

Then, with ($i = \gamma, Z$), and after inserting the ordinary EM (γ) charges for the u, d, and s quarks [$e^\gamma = +2/3\,(u), -1/3\,(d,s)$], as well as the weak quark charges [$e^Z = 1 - 8/3\,\sin^2\theta_W\,(u), -1 + 4/3\,\sin^2\theta_W\,(d,s)$], it follows straightforwardly that

$$G_{E,M}^{pZ} = \left(1 - 4\sin^2\theta_W\right) G_{E,M}^{p\gamma} - G_{E,M}^{n\gamma} - G_{E,M}^{s\gamma} = Q_W^p\, G_{E,M}^{p\gamma} - G_{E,M}^{n\gamma} - G_{E,M}^{s\gamma}. \quad 10.$$

Inserting Equation 10 into Equation 2, we can write the asymmetry in terms of the proton's weak charge Q_W^p and its extended structure expressed in terms of EM (A_{EM}), strange quark (A_s), and

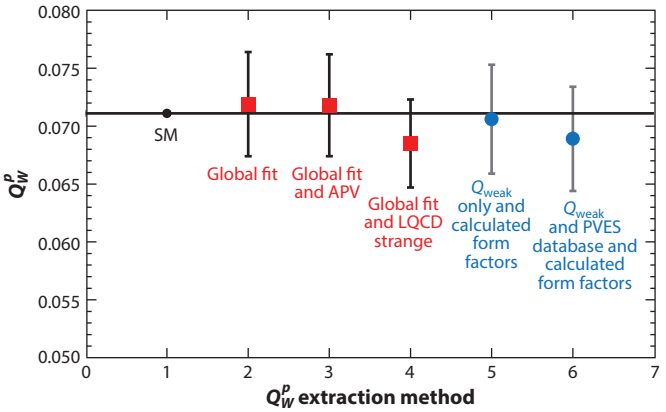

Figure 2

The values of the proton's weak charge determined from each of several methods are compared with one another and with the SM prediction (labeled method 1). The red points show weak-charge results determined from global fits incorporating the Q_{weak} asymmetry datum together with the PVES database (method 2), the same including the APV weak-charge result (method 3), or a variant of method 2 that constrains the strange form factors $G_{E,M}^s$ using LQCD calculations (method 4). The first blue point (method 5) uses only the Q_{weak} asymmetry datum with calculated (instead of fitted) axial and lattice strange form factors. The second blue point (method 6) extends method 5 to include the $\vec{e}p$ PVES database. Abbreviations: APV, atomic parity violation; LQCD, lattice quantum chromodynamics; PVES, parity-violating electron scattering; SM, Standard Model.

axial (A_{ax}) components as

$$A/A_0 = Q_W^p - (A_{EM} + A_s + A_{\text{ax}}), \quad \text{where} \tag{11.}$$

$$A_{EM} = A_E + A_M = \left(\varepsilon \left(G_E^p G_E^n\right)^2 + \tau \left(G_M^p G_M^n\right)^2\right)/D, \tag{12.}$$

$$A_s = A_E^s + A_M^s = \left(\varepsilon \left(G_E^p G_E^s\right)^2 + \tau \left(G_M^p G_M^s\right)^2\right)/D, \tag{13.}$$

$$A_{\text{ax}} = \varepsilon' \left(1 - 4\sin^2\theta_{\text{W}}\right)^2 G_M^p G_A^e/D, \quad \text{and} \tag{14.}$$

$$D = \varepsilon \left(G_E^p\right)^2 + \tau \left(G_M^p\right)^2. \tag{15.}$$

The kinematic factors ε and ε' (defined in Equation 3) have numerical values close to one and zero, respectively, near the forward-angle kinematics of the Q_{weak} experiment. As noted in Section 1.2, in this forward-angle limit the asymmetry in Equation 11 can be expressed as in Equation 4, similar to the slope-intercept form of a line $y(x) = mx + b$, where $y(x) = A/A_0$ (both A and A_0 are functions of $x = Q^2$), the intercept $b = Q_W^p$, and the slope $m = B(Q^2, \theta)$ are themselves functions of $x = Q^2$:

$$A/A_0(Q^2) = Q_W^p + Q^2 B(Q^2, \theta). \tag{16.}$$

The intercept Q_W^p is a fundamental property of the proton and so is independent of Q^2. The slope $B(Q^2, \theta)$ encapsulating the nucleon structure in terms of the neutron and proton EM form factors $G_{E,M}^{p,n}$ and weak neutral form factors $G_{E,M}^s$ and G_A described in Equations 12–15 is constrained by PVES data at higher Q^2. As noted in Section 1.2, the weak neutral form factors are suppressed relative to Q_W^p at lower Q^2, and the asymmetry A decreases with Q^2 while the elastic scattering cross section increases as $(1/Q^2)^2$. The global fit method uses Equation 11 to determine Q_W^p from

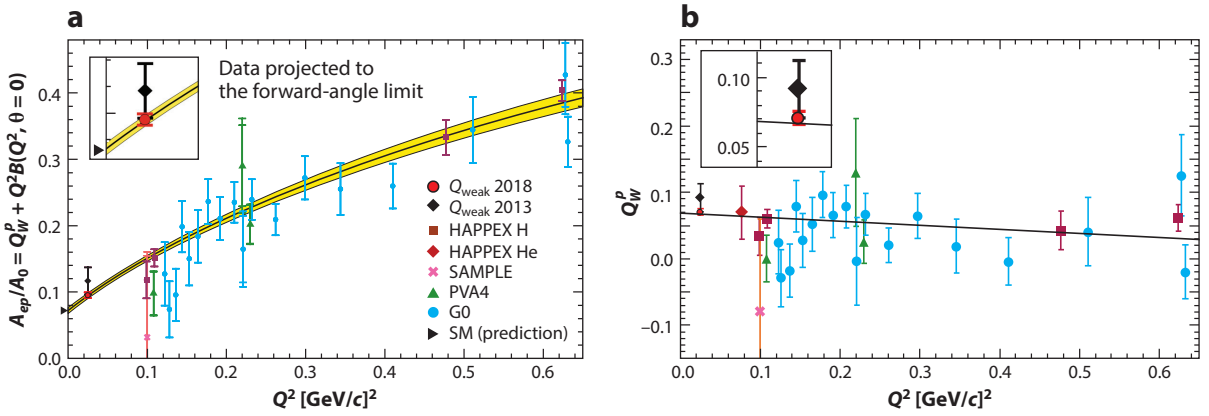

Figure 3

(*a*) Global fit (*black curve*) of the reduced asymmetries A/A_0 constituting the parity-violating electron-scattering (PVES) database, obtained by varying the weak vector quark couplings C_{1u} and C_{1d}, the strength of the strange form factors $G_{E,M}^s$, and the isovector axial form factor $G_A^{Z(T=1)}$. The yellow band indicates the uncertainty in the fit. (*Inset*) The region of the Q_{weak} experiment that dominates the fit. The legend indicates the different collaborations responsible for the data used in the fit as well as the Standard Model (SM) value of Q_W^p with the black arrowhead at $Q^2 = 0$. (*b*) A linear fit (*black line*) is made to the Q_W^p obtained for each datum in the PVES database by calculating A_{EM}, A_s, and A_{ax} in Equation 11 for each measured asymmetry. Panel *a* adapted from Reference 8.

the intercept of a fit of A/A_0 versus Q^2. Therefore, asymmetry measurements at lower Q^2 have the advantage that the extrapolation to the intercept at $Q^2 = 0$ is shorter and the experiment's rates are higher, although the asymmetries are smaller and more challenging to measure. **Figure 3*a*** shows the result of the global fit reported in Reference 8. To make this figure tractable, the $\vec{e}p$ reduced asymmetries were rotated to $\theta = 0^\circ$, as described in Reference 32. The fit varied six parameters: $C_{1u}, C_{1d}, G_A^p, G_A^n$, and the overall magnitudes ρ_s and μ_s of the strange electric and magnetic form factors G_E^s and G_M^s. The small isoscalar combination of the axial form factors $G_A^{Z(T=0)} = (G_A^p + G_A^n)/2$ was constrained by the calculation in Reference 34, leaving five effective parameters in the fit. A dipole form $G_D = (1 - Q^2/\lambda^2)^{-2}$ with $\lambda = 1$ GeV^2 was used to describe the Q^2 dependence of G_A. The strange form factors were taken to be $G_E^s = \rho_s Q^2 G_D$ and $G_M^s = \mu_s G_D$, following Reference 47. The fit was truncated at $Q^2 = 0.63$ GeV^2 in order to avoid nearly doubling the Q^2 reach only to include two additional asymmetries (25) at $Q^2 = 0.79$ and 1.00 GeV^2 with large uncertainties, which have a negligible impact on the outcome of the fit.

The intercept of the global fit, $Q_W^{gf}(p) = 0.0719 \pm 0.0045$, agrees well with the SM prediction, $Q_W^{SM}(p) = 0.0711 \pm 0.0002$ (provided in table 10.4 of Reference 35). Note that the SM prediction of Q_W^p has improved slightly relative to that reported in Reference 8 due to recent improvements in our knowledge of (mainly) the masses of the top quark and the Higgs boson (35).

An energy dependence is implicit in $B(Q^2, \theta)$ because $Q^2 \sim 4E_f E_i \sin^2\theta/2$. As a result, the energy dependence of the one electroweak radiative correction that depends on energy (the $\Box_{\gamma Z}$) has to be accounted for. As described in References 8 and 32, the $\vec{e}p$ reduced asymmetries A/A_0 in the PVES database are corrected for the energy dependence of the vector piece (the largest piece) (36) and axial-vector piece (37, 38) of the γZ box radiative correction $\Box_{\gamma Z}^{VAV}$, as well as a small Q^2 correction (44) to $\Box_{\gamma Z}$. At the kinematics of the Q_{weak} experiment, the combined correction is 0.0046(5), or 6.4% ± 0.6% of Q_W^p. Several theoretical groups (39–43) employing slightly different approaches and experimental constraints generally agree on the central value of $\Box_{\gamma Z}^V$ at the kinematics of the Q_{weak} experiment, but differ on the theoretical uncertainty of this correction (**Figure 4*a***). Despite several workshops dedicated to resolving the predicted

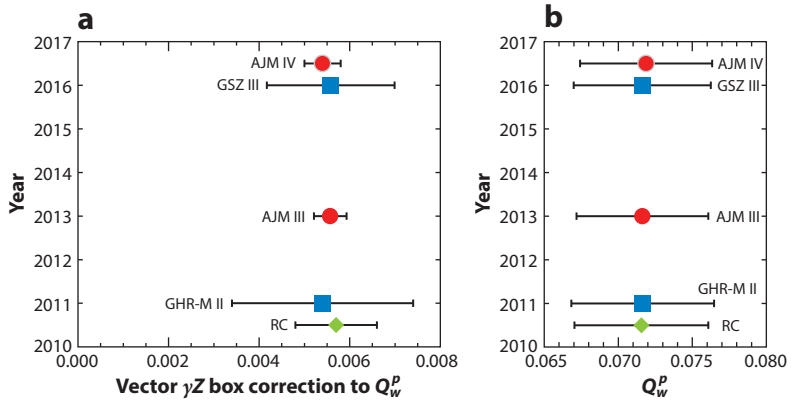

Figure 4

(*a*) Calculations of the energy dependence of the vector piece of the γZ box radiative correction from three groups since 2011. Blue squares represent calculations by Gorchtein et al. (39, 40); green diamonds, Rislow & Carlson (41); and red circles, the AJM (Adelaide–JLab–Manitoba) Collaboration (42, 43). (*b*) Determinations of the proton's weak charge using the global fit method for each of the calculated $\Box_{\gamma Z}^{V}$ radiative corrections in panel *a*.

discrepancies,[1] to date no consensus has been achieved. However, at the present level of uncertainty achieved for Q_W^p, the differences in the various calculations of the $\Box_{\gamma Z}$ correction and its uncertainty correspond to negligible changes in the result quoted for Q_W^p. This conclusion was arrived at by carrying out global fits employing each of the γZ box predictions in turn (the results for each are shown in **Figure 4*b***).

Reference 8 also explored what happens when the strange form factors $G_{E,M}^s$ are constrained to the predictions of lattice quantum chromodynamics (LQCD) calculations (45) instead of being floated in the fit to the PVES data. This reduces the number of effective parameters in the global fit from five to three. The motivation is threefold. First, the LQCD calculations have improved to the point that they are near (45) or even at (46) the physical pion mass. The uncertainties for $G_{E,M}^s$ reported in the LQCD calculations are tiny (less than one-twentieth of what we can currently determine from fits to experimental data). Second, the best experimental constraints on $G_{E,M}^s$ come from the higher-Q^2 data in the PVES database where $G_{E,M}^s$ are largest. But those data have larger uncertainties in general than those at lower Q^2, and are subject to fundamentally different backgrounds, such as hyperon production and decay, that the experiments had to take into account (25). Finally, we know already (45) that there is slight tension at roughly the 1σ level between the strange form factors extracted either from the PVES data or from LQCD calculations. Not knowing a priori which is more appropriate, we explore both.

With $G_{E,M}^s$ constrained to the LQCD predictions (and uncertainties), the global fit returns $Q_W^{\mathrm{LQCD}}(p) = 0.0685 \pm 0.0038$. This shift of 0.0034 from the primary Q_{weak} result $Q_W^{\mathrm{gf}}(p)$ amounts to a shift of 0.58σ (0.76σ), assuming that the uncertainties are completely uncorrelated (correlated), consistent with the same level of tension apparent in Reference 45. The smaller uncertainty in the $Q_W^{\mathrm{LQCD}}(p)$ result is due to the dramatically smaller $G_{E,M}^s$ uncertainties in the LQCD $G_{E,M}^s$ calculations relative to those determined from the PVES data in the global fit. Interestingly, the shape of $G_{E,M}^s$ (the Q^2 dependence) calculated from the lattice looks very similar to that assumed

[1]See **https://www.jlab.org/conferences/gz-box/program.html** and **https://www.physics.umass.edu/acfi/seminars-and-workshops/the-electroweak-box**.

for the global fit, which was explored and optimized in much earlier research (47). The magnitude of both G_E^s and G_M^s in the LQCD calculations is approximately one-tenth of that determined from the global fit, but the behavior with Q^2 is about the same.

3.2. Determining Q_W^p from the Q_{weak} Datum and Calculated Form Factors

In the global fit discussed above, the record-breaking precision and proximity to $Q^2 = 0$ of the Q_{weak} experiment's final result clearly dominate the outcome of the fit. The fit is essentially forced to go through the very precise Q_{weak} datum, although the slope at that point is determined from the higher-Q^2 PVES data. With that in mind, it is interesting to ask the question: What Q_W^p would result from using the Q_{weak} datum by itself?

Without the benefit of the other data in the PVES database to determine the hadronic structure $B(Q^2, \theta)$ term in Equation 16, that term would instead have to be calculated in order to interrogate the Q_W^p implied from the Q_{weak} datum alone. However, extrapolation to $Q^2 = 0$ would be unnecessary, since from Equation 16 it is obvious that $Q_W^p = Q^2 B(Q^2, \theta) - A/A_0(Q^2)$. In other words, the two terms on the right side of the equation (each of which depends on Q^2) must conspire to give the Q^2-independent result (Q_W^p) on the left side of the equation.

Further motivating the effort to extract Q_W^p from the Q_{weak} result alone is the fact that at the low Q^2 of the Q_{weak} experiment ($Q^2 = 0.0248$ GeV^2), the contributions from A_s and A_{ax} to the $B(Q^2, \theta)$ term are small. In Reference 8, $A_{E,M}$ were taken from the parameterization of the nucleon EM form factors $G_{E,M}^{p,n}$ from Reference 33. The $A_{E,M}^s$ terms were formed from the LQCD calculations of $G_{E,M}^s$, referred to above, from Reference 45. The axial piece, A_{ax}, was calculated using the prescription and input for G_A found in Reference 48. The theoretical uncertainties reported in those three articles were taken fully into account in this stand-alone determination of Q_W^p from the Q_{weak} datum. For example, the uncertainty in A_E^s at each Q^2 is

$$\Delta A_E^s = \sqrt{\left(\frac{\partial A_E^s}{\partial G_E^p}\right)^2 (\Delta G_E^p)^2 + \left(\frac{\partial A_E^s}{\partial G_E^s}\right)^2 (\Delta G_E^s)^2 + \left(\frac{\partial A_E^s}{\partial G_M^p}\right)^2 (\Delta G_M^p)^2}, \qquad 17.$$

where the derivatives were taken using Equation 13 and the Q^2-dependent form factor uncertainties were taken from References 33 and 45 for $\Delta G_{E,M}^p$ and ΔG_E^s, respectively. The correction applied for the energy dependence of the γZ box radiative correction (and its uncertainty) was the same as described in Section 3.1. Each of these contributions to $Q^2 B(Q^2, \theta)$ was calculated at the Q^2 of the Q_{weak} experiment, and the results are presented in **Table 2**.

The result is $Q_W^{\text{sa}}(p) = 0.0706 \pm 0.0047$, where the superscript refers to this stand-alone determination using only the Q_{weak} datum. It lies just 0.2σ below the primary result reported in Section 3.1. Since it makes use of the lattice $G_{E,M}^s$, the result might be expected to drop because that is what happened when the lattice results for $G_{E,M}^s$ were used in the global fit. The reason the drop in Q_W^p is smaller for the stand-alone result than it was for the global fit is likely because $G_{E,M}^s$ is smaller at the Q^2 of the Q_{weak} result than it is for any other datum in the PVES database. Note also that the uncertainty of the Q_W^p result extracted from the Q_{weak} experiment's datum alone is almost the same as that extracted using the global fit and the entire PVES database.

The advantages of the stand-alone result include its simplicity and transparency. It is easy to use **Table 2** to estimate the impact on Q_W^p from various effects. One such effect of contemporary interest is the proton-radius puzzle (49, 50), so named because the proton radius determined from electron-scattering data disagrees by up to 7σ from that determined from muonic Lamb-shift measurements. Since the determination of Q_W^p relies on our knowledge of G_E^p and, therefore, indirectly on $r_p = <r_E^2>^{1/2}$, it is reasonable to ask what impact this ambiguity in r_p has on the

Table 2 Ingredients in the determination of Q_W^p from the Q_{weak} datum alone

Ingredient	Value (ppb)	Error (ppb)	Value/total (%)
A_E	−26.20	3.63	12%
A_M	79.88	1.36	35%
A_E^s	−1.11	0.33	0%
A_M^s	0.77	0.24	0%
A_{ax}	5.60	2.36	2%
A_{had} total	58.95	4.55	26%
Q_{weak} A	−226.50	9.30	100%
A_{had}+ Q_{weak}	−167.55	10.35	74%
A_0	−2,229.33		
Q_W^p	0.0752	0.0046	107%
γZ box	0.0046	0.0005	7%
Q_W^p–γZ	0.0706	0.0047	100%

determination of Q_W^p. There are many different experiments available to characterize the magnitude of the proton-radius puzzle, but two typical examples are an electron-scattering data global analysis (51), which finds $r_p(ep) = 0.875 \pm 0.010$ fm, and a muonic Lamb-shift result (52), which returns $r_p(\mu p) = 0.8409 \pm 0.0004$ fm. The difference is $\Delta r_p = 0.034$ fm, or 3.4σ. The impact of this difference on Q_W^p can be estimated from the familiar $Q^2 \to 0$ Taylor-series expansion:

$$G_E \sim Z\left(1 - Q^2 < r^2 > /6 + \ldots\right). \qquad 18.$$

This equation says that at the low Q^2 of the Q_{weak} experiment, the two different values of r_p imply $G_E(ep) \sim 0.9178$ and $G_E(\mu p) \sim 0.9241$—that is, a $\Delta G_E = 0.7\%$. According to **Table 2**, G_E contributes −26.2 ppb to the hadronic structure asymmetry, so the shift in asymmetry implied by the proton-radius puzzle is $\Delta A \sim (0.7\%)$ (26 ppb) ∼0.2 ppb out of the −226.5 ppb measured in that experiment. Then, the estimated shift in Q_W^p due to the proton-radius puzzle is $\Delta Q_W^p \sim \Delta A/A_0 = 0.00008$, or 2% of the Q_{weak} uncertainty (only 0.1% of the Q_{weak} central value). We can therefore conclude that the effect of the proton-radius puzzle on the determination of Q_W^p is completely negligible.

Another effect apparent from **Table 2** that is pertinent to future higher-precision experiments is the size of the uncertainties associated with the hadronic structure contributions. In this table, the contributions from $A_{E,M}^{p,n}$, $A_{E,M}^s$, and A_{ax} are added in quadrature. But the contributions from the uncertainties in G_E^p, G_E^n, G_M^p, and G_M^n that contribute to $A_{E,M}^{p,n}$ are also assumed to be uncorrelated, because the correlations are not reported in the literature. Therefore, the uncertainties associated with the EM form factors $A_{E,M}^{p,n}$ are overestimated in the stand-alone method.

In the global fit described in Section 3.1, above, this problem was dealt with (8) by performing the fit with a variety of different EM form factor parameterizations (33, 53–55) and folding the full range of variation observed in Q_W^p into the uncertainty of the weak-charge result. That estimation of the uncertainty associated with the EM form factors was approximately 1%, only a small additional contribution to the uncertainty reported in the Q_{weak} experiment.

3.3. Q_W^p from the Q_{weak} Datum, Parity-Violating Electron-Scattering Database, and Calculated Form Factors

The successful extraction of the weak charge described above using only the Q_{weak} datum prompts the question of whether this technique could be extended to the entire PVES database. What

Section 3.2 essentially found is that since Q_W^p is independent of Q^2, it can be determined from any datum in the PVES database. Obviously, the place to start is with the datum closest to threshold and with the highest precision. In this section, however, we explore what happens if we determine a Q_W^p for each measured asymmetry in the PVES database by calculating $(A_{E,M})$, $A_{E,M}^s$, and $A_{\rm ax}$ for each datum, and fitting the resulting weak charges with a straight line as a function of Q^2. Since the Q_W^p determined in this manner for each datum should be the same number (within our ability to calculate the hadronic structure terms $A_{E,M}^s$ and $A_{\rm ax}$), the fit should be a straight line with a small and constant slope. This would stand in contrast to the situation for the global fit described in Section 3.1, where the fit had a relatively steep slope, especially in the extrapolation region.

In Section 3.1, it was important to include the $\vec{e}d$ data (19, 23, 24, 26) to constrain $A_{\rm ax}$, and to include $\vec{e}\,^4$He data (29, 30) to constrain A_E^s in particular, when fitting the PVES data, which comprise mostly $\vec{e}p$ elastic asymmetries. But since we are going to calculate $A_{\rm ax}^s$ and $A_{E,M}^s$ for this linear-fit method, those data are not so helpful. They mostly measure the neutron's weak charge and are not very sensitive to the much smaller proton weak charge. Using the same lattice calculations and axial calculations as employed in Section 3.2, the weak charges were determined from each datum in the $\vec{e}p$ database (20–23, 25–28, 30, 31) and are plotted in **Figure 3*b***, along with the linear fit to these results. The more precise of the two $\vec{e}\,^4$He results is also included but has negligible impact on the fit. Clearly, the slope of the fitted line is reasonably shallow relative to the global fit in **Figure 3*a***. The intercept of the fit is $Q_W^{\rm sl}(p) = 0.0689 \pm 0.0045$, where the superscript denotes the straight-line fit. This value agrees almost exactly with the lattice result obtained in the global fit: $Q_W^{\rm LQCD}(p) = 0.0685 \pm 0.0038$.

Both the straight-line and LQCD results are 0.6σ lower than the global fit, whereas the stand-alone fit is only 0.2σ lower, supporting the explanation that the $G_{E,M}^s$ in the higher-Q^2 PVES data are what drag down the result in the straight-line and LQCD results. There appears to be some slight tension between the fit strange and lattice strange form factors at higher Q^2.

4. THE RUNNING OF $\sin^2\theta_{\rm w}$

The most convenient way to compare precision neutral-current measurements is through values of the weak mixing angle, $\sin^2\theta_{\rm w}$, extracted from each measurement. The weak mixing angle characterizes the mixing of the two neutral currents (EM and neutral weak) in the SM. Neutral-current experiments have measured the decays of directly produced Z^0 bosons at or near the Z^0 mass as well as the effects of virtually exchanged Z^0 bosons at energy scales well below the Z^0 mass. Expressions for each of the experimental observables that include all quantum corrections at the one-loop level can be used to extract a value of $\sin^2\theta_{\rm w}$ for each measurement (details of this extraction procedure for the $Q_{\rm weak}$ experiment can be found in Reference 8). **Figure 5** shows the extracted values for the most precise measurements at and below the Z^0 mass. The theoretical prediction for how $\sin^2\theta_{\rm w}$ evolves with energy scale Q—often referred to as the running of the weak mixing angle—is also shown (56–58) as the curve in **Figure 5**. This evolution from the Z pole is calculated using the renormalization-group equation procedure in the modified minimal subtraction ($\overline{\rm MS}$) scheme. The relative theoretical precision of this curve is $\pm 0.01\%$ at Q corresponding to the Z boson mass from a global fit to the SM, with an additional evolution uncertainty from hadronic effects of $\pm 0.01\%$ at $Q = 0$ (57).

The Z^0 pole measurements (35) in **Figure 5** come from several measurements at LEP1, with the forward–backward asymmetry $A_{\rm FB}$ from $Z \to b\bar{b}$ being the most precise; the left–right Z pole production asymmetry $A_{\rm LR}$ measurement at the SLAC/Stanford Linear Collider (SLC); and the forward–backward asymmetry measurements of Drell–Yan lepton pairs at the Tevatron and LHC. The most precise measurements at low energy are all weak-charge measurements, with the

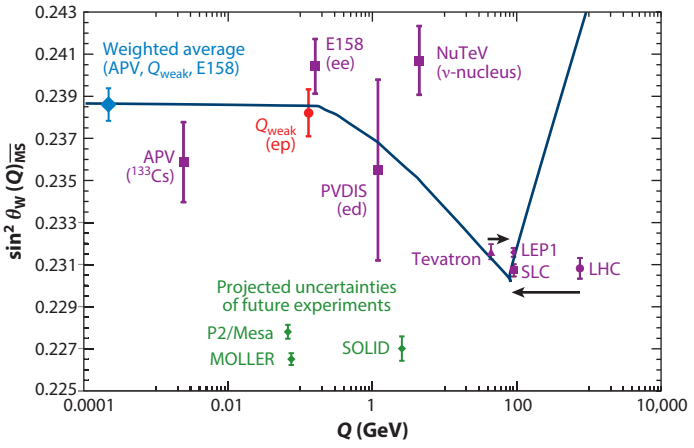

Figure 5

Variation of $\sin^2\theta_w$ with energy scale Q. The modified minimal subtraction ($\overline{MS}$) scheme prediction of the Standard Model is shown as a solid curve, along with existing experimental determinations and some proposed future measurements. Refer to References 7, 8, 19, 23, 24, 26, 29, 30, 56–58, 60, and 61–64. The weighted average of the three low-Q weak-charge measurements is displayed at arbitrary Q to indicate the confirmation of the running of the weak mixing angle with 9.6σ significance. Figure adapted from Reference 8.

Q_{weak} measurement completing the weak-charge triad (59), which includes the weak-charge measurements of the electron in PV Møller scattering (SLAC E158) (7), ^{133}Cs (dominated by the weak charge of the neutron) from atomic parity violation (APV) (60, 61), and the proton from Q_{weak} (8).

Both the weak charge of the electron and that of the proton are suppressed in the SM [both ($1-4\sin^2\theta_w$) to first order], while the weak charge of ^{133}Cs, which is dominated by the neutron's weak charge, has no such suppression. Consequently, a much more precise relative uncertainty on the ^{133}Cs measurement is required for similar precision on the weak mixing angle. Specifically, relative precision on the weak-charge measurements of 13%, 6.3%, and 0.59% for the electron, proton, and ^{133}Cs are required for relative precision on $\sin^2\theta_w$ of 0.54%, 0.47%, and 0.81%, respectively. Within the precision of these measurements, the SM predicts a constant value of the weak mixing angle in this low-energy region. Testing the hypothesis that these three measurements are consistent with a constant results in a χ^2 per degree of freedom of 1.90, corresponding to a probability of 0.149. Thus, it is reasonable to combine the points to obtain the weighted-average point shown in **Figure 5**. The predicted SM running of $\sin^2\theta_w$ from the Z pole to $Q = 0$ is a relative change of approximately 3.2%. Use of the weighted-average value confirms this change with 9.6σ significance.

All of the measurements are consistent at the $<2\sigma$ level with the SM, with the exception of the NuTeV result (62) from neutrino–nucleus scattering. It has been argued (63) that this 3σ discrepancy may be attributed in part to substantial unaccounted-for nuclear physics effects, including neutron-excess corrections to the quark momenta, charge-symmetry breaking, and strange quark momentum asymmetries. When estimates of these effects are included, the $\sin^2\theta_w$ value from NuTeV comes into agreement with the SM prediction.

The most precisely determined data points shown in **Figure 5** are from the Z pole. However, the low-energy points with more modest precision have better sensitivity to certain types of BSM physics because they are well away from the Z pole. This enhanced sensitivity is due in part to heavy New Physics such as additional heavy Z' bosons, or leptoquarks, that can generally be

described by an effective low-energy four-fermion contact interaction, as discussed in Section 5. The contribution of such interactions is heavily suppressed at the Z pole due to the lack of an interference term (64). This can be understood by inspecting the amplitudes for the exchanges of a Z boson and New Physics characterized by an exchange particle of mass Λ and decay width $\Gamma_{\rm new}$:

$$A_Z \propto \frac{1}{q^2 - M_Z^2 + iM_Z\Gamma_Z}, \quad A_{\rm new} \propto \frac{1}{q^2 - \Lambda^2 + i\Lambda\Gamma_{\rm new}}. \tag{19.}$$

At the Z pole ($q^2 = M_Z^2$), A_Z is purely imaginary and the New Physics amplitude is dominantly real in the situation where $\Lambda \gg M_Z, \Gamma_{\rm new}$. Thus, there is no interference term between the Z and New Physics terms in the amplitude:

$$|A_Z + A_{\rm new}|^2 = A_Z^2 \left[1 + \left(\frac{A_{\rm new}}{A_Z}\right)^2 + \ldots\right]. \tag{20.}$$

By contrast, at low energies ($q^2 \ll M_Z^2$), both amplitudes are dominantly real and there is an interference term:

$$|A_Z + A_{\rm new}|^2 = A_Z^2 \left[1 + 2\left(\frac{A_{\rm new}}{A_Z}\right) + \ldots\right]. \tag{21.}$$

Since we are considering the case $\Lambda \gg M_Z$, and therefore $A_{\rm new} \ll A_Z$, the New Physics makes a much larger relative contribution to the observable at low energy than on the Z pole.

Future experiments are also shown in **Figure 5**. Improved precision measurements on the weak charges of the proton (65) and electron (66) are planned. In addition, there are plans to improve the existing PV deep-inelastic scattering datum (67) using a new approach (68, 69). Several efforts are also being pursued for improved APV experiments (a summary can be found in Reference 58).

5. THE SEARCH FOR PHYSICS BEYOND THE STANDARD MODEL

The weak-charge result can be used to set limits on potential new BSM physics. In principle, the New Physics might not couple to the same *uud* combination of quark flavors found in the proton. In order to allow the New Physics to couple to arbitrary (valence) quark flavors, we define a flavor-mixing angle

$$\theta_b = \tan^{-1}(N_d/N_u), \tag{22.}$$

as in Reference 70. For the proton, $N_d = 1$, $N_u = 2$, and $\theta_b = 26.6^\circ$. Then, the u and d quark components can be expressed as

$$b_V^u = \cos\theta_b \text{ and } b_V^d = \sin\theta_b. \tag{23.}$$

Let q represent the quark flavor, and C_{1q} the vector quark couplings. Then, new PV SL four-point contact interaction BSM physics can be introduced in the Lagrangian in a completely general (model-independent) way with a new contact interaction characterized by mass scale Λ and coupling g. The measured PV Lagrangian $\mathscr{L}_{\rm PV}^{\rm msrd}$ can be expressed as the sum of the SM neutral-current Lagrangian $\mathscr{L}_{\rm NC}^{\rm SM}$ and the PV piece $\mathscr{L}_{\rm PV}^{\rm new}$ associated with new BSM physics:

$$\mathscr{L}_{\rm PV}^{\rm msrd} = \mathscr{L}_{\rm NC}^{\rm SM} + \mathscr{L}_{\rm PV}^{\rm new} \tag{24.}$$

$$= \bar{e}\gamma_\mu\gamma_5 e \sum_q \left(\frac{G_{\rm F}}{\sqrt{2}} C_{1q} + \frac{g^2}{\Lambda^2} b_V^q\right) \bar{q}\gamma^\mu q. \tag{25.}$$

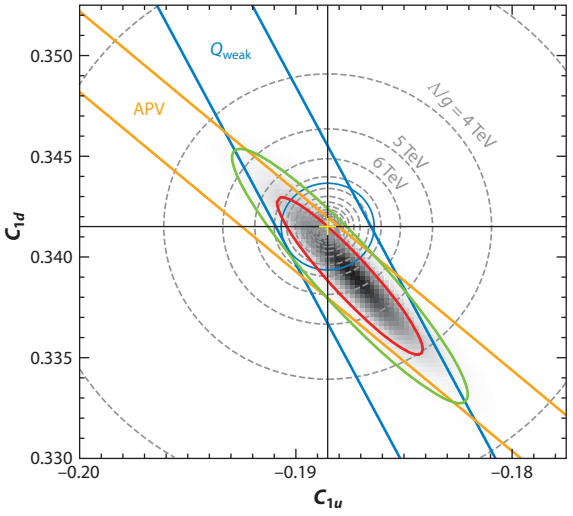

Figure 6

Contours of Λ/g in C_1 space. The yellow cross indicates the Standard Model origin. The dashed circles represent mass-reach contours, starting with $\Lambda/g = 3$ TeV (outermost, incomplete contour), which increase in steps of 1 TeV at progressively smaller diameters. The 95%-CL constraints provided by the Q_{weak} and atomic parity-violation (APV) experiments are shown as blue and orange bands, respectively. The 68%- and 95%-CL combined constraints from these two experiments are shown as red and green ellipses, respectively. The solid blue circle indicates the 95%-CL constraint provided by the Q_{weak} experiment on the proton. Figure adapted from Reference 8.

By rearranging and carrying out the sum using Equation 23, we can recast Equation 25 in terms of the vector quark charges C_{1q} as follows:

$$\left(C_{1u}^{\text{msrd}}, C_{1d}^{\text{msrd}}\right) = \left(C_{1u}^{\text{SM}}, C_{1d}^{\text{SM}}\right) + r\,(\cos\theta_b + \sin\theta_b). \quad 26.$$

This is simply the polar form of a circle in C_{1q} space centered at the SM value of the vector quark charges $\left(C_{1u}^{\text{SM}}, C_{1d}^{\text{SM}}\right)$, with radius

$$r = \frac{\sqrt{2}}{G_F}\left(\frac{g}{\Lambda}\right)^2. \quad 27.$$

These circles describe contours of different mass sensitivity Λ/g in C_{1q} space (**Figure 6**).

5.1. Constraints Provided by Weak-Charge Experiments

The constraint (at tree level[2]) provided by the Q_{weak} experiment in C_{1q} space is the band defined by the two lines

$$Q_W(p) \pm \Delta Q_W(p) = -2(2C_{1u} + C_{1d}). \quad 28.$$

The mass reach associated with the Q_{weak} experiment alone can be read directly from **Figure 6** or computed geometrically as the distance between the SM origin and the lines defining the perimeter of the Q_{weak} band. The distance between the line $Ax + By + C = 0$ and the point

[2]See equation 10.30 of Reference 35 for the full expression, including radiative corrections.

$(C_{1u}^{\rm SM}, C_{1d}^{\rm SM}) = (-0.18853, 0.34151)$ is

$$d = \frac{AC_{1u}^{\rm SM} + BC_{1d}^{\rm SM} + C}{\pm\sqrt{A^2 + B^2}}, \qquad 29.$$

where, in the case of $Q_W(p)$, we have $A = -4$, $B = -2$, and $C = Q_W(p) \pm \Delta Q_W(p) = 0.0719 \pm 0.0045$, and Λ/g is determined from this distance d using Equation 27. The larger of these two distances is related via Equation 27 to the minimum mass reach below which new PV SL BSM physics is excluded for the proton by the $Q_{\rm weak}$ experiment: $\Lambda/g = 7.5$ TeV (95% CL). For the value (71) of $g^2 = 4\pi$ typically chosen to make comparisons between different experiments (72), this implies a mass reach of $\Lambda = 26.6$ TeV (95% CL) for the $Q_{\rm weak}$ experiment. Note that the slope of the lines defining the $Q_{\rm weak}$ band (-2) means that the slope of a line perpendicular to the band is $+1/2$, which corresponds to the $\theta_b = 26.6^\circ$ flavor-mixing angle of the proton (see Equation 22).

The intuitive geometrical analysis described above makes use of the measured weak charge and the SM values for the vector weak couplings. Alternatively, precisely the same results may be obtained by comparing the measured and SM values of the weak charge, as in Reference 8:

$$\frac{\Lambda_\pm}{g} = v\sqrt{\frac{4\sqrt{5}}{|Q_W^p \pm 1.96\Delta Q_W^p - Q_W^{\rm SM}|}}, \qquad 30.$$

where $v = 1/\sqrt{\sqrt{2}G_{\rm F}} = 0.24622$ TeV is the electroweak (Fermi) scale and represents the vacuum expectation value of the Higgs field. The lesser of the two values described in Equation 30 is $\Lambda_+/g = 7.5$ TeV, using $Q_W^{\rm SM}(p) = 0.0711$ from table 10.4 in Reference 35. It agrees with the geometric result obtained using Equation 29.

The only other high-precision SL weak-charge measurement (60) was performed on cesium (^{133}Cs), although experiments with less precision have also been published for thallium (74), bismuth (75), and lead (76). The APV results (60, 61, 73) also provide constraints (bands) in C_{1q} space since, for a system of Z protons and N neutrons (at tree level), the weak charge can be expressed as (35)

$$Q_W(Z,N) = -2\,[(2Z+N)C_{1u} + (Z+2N)C_{1d}]. \qquad 31.$$

Using the most recent atomic corrections (61) to the cesium result (60, 73), we find

$$Q_W(^{133}{\rm Cs}) = -2(188C_{1u} + 211C_{1d}) = -72.62 \pm 0.43. \qquad 32.$$

By combining this result with Equation 29, we can determine a mass reach for the ^{133}Cs APV band the same way we did for the $Q_{\rm weak}$ experiment's band. We find that the mass reach associated with the ^{133}Cs APV band is $\Lambda/g = 6.9$ TeV (95% CL).

The combined constraints from $Q_{\rm weak}$ (ep) and APV (^{133}Cs) on the vector weak charges C_{1u} and C_{1d} are defined by the ellipse

$$\Delta\chi^2 = \left(\frac{Q_W^{\rm APV}(X,Y) - Q_W^{\rm APV}({\rm msrd})}{\Delta Q_W^{\rm APV}({\rm msrd})}\right)^2 + \left(\frac{Q_W^p(X,Y) - Q_W^p({\rm msrd})}{\Delta Q_W^p({\rm msrd})}\right)^2. \qquad 33.$$

Here, $\Delta\chi^2 = 5.99$ for 95% CL (see table 39.2 of Reference 35). $Q_W^{\rm APV}(X,Y)$ and $Q_W^p(X,Y)$ refer to Equation 31 for ^{133}Cs (APV) and the proton ($Q_{\rm weak}$) with $(X,Y) = (C_{1u}, C_{1d})$. The values $Q_W({\rm msrd})$ and the uncertainties $\Delta Q_W({\rm msrd})$ of the weak charges measured for ^{133}Cs and the proton are taken from table 10.4 of Reference 35. **Figure 6** shows the 95%-CL constraints as

bands, defined by the Q_{weak} and APV weak-charge measurements, as well as the 95%-CL ellipse defined by combining both bands, along with different Λ/g contours.

5.2. Flavor-Independent Constraints

The mass reaches quoted above for Q_{weak} (ep) and APV (^{133}Cs) are specific to the proton and ^{133}Cs, respectively. But there is no reason to assume that the new and unknown BSM physics would necessarily couple to the specific flavor ratios of those two systems. The New Physics might couple only to u quarks or only to d quarks, or some other combination. To obtain a completely general result, we seek a mass reach that is independent of what flavors the New Physics couples to.

The ellipse in **Figure 6** shows the most likely region at 95% CL to find any of a generic class of BSM physics models parameterized by Λ/g and θ_b. It is tempting to associate the point on this ellipse farthest from the SM origin with the minimum Λ/g for any given θ_b, in other words, a θ_b-independent mass limit for BSM physics. But the ellipse is by definition a two-parameter entity, and we seek a one-parameter solution. Once we pick a θ_b, we are simply considering a single slice through the parameter space.

Mass limits appropriate to a specific choice of the flavor-mixing angle θ_b can be obtained by considering a line of constant θ_b through the SM origin. Since only the parameter Λ/g varies along fixed θ_b, the distance from the SM origin (radius) along this line corresponding to $\Delta\chi^2 = 3.84$ about the local χ^2 minimum is the 95%-CL limit on Λ/g for that particular value of θ_b. In practice, we choose a specific θ_b and proceed as follows: First, the radius r_{min} associated with the local χ^2 minimum $\chi^2_{\text{min}}(\theta_b)$ is identified by setting the derivative $\partial(\Delta\chi^2)/\partial r$ of Equation 33 to zero with $(X, Y) = (r\cos\theta_b, r\sin\theta_b)$. We then obtain $\chi^2_{\text{min}}(\theta_b)$ from Equation 33 with $(X, Y) = (r_{\text{min}}\cos\theta_b, r_{\text{min}}\sin\theta_b)$. Then, Equation 33 is solved for r with $\Delta\chi^2 = [\chi^2_{\text{min}}(\theta_b) + 3.84]$ at the specific θ_b under consideration. That radius corresponds to a 95%-CL Λ/g for that choice of θ_b via Equation 27. Carrying out this procedure for all values of θ_b results in the mass-limit curve as a function of θ_b (**Figure 7*a***). The minimum Λ/g on that curve is 3.6 TeV, the θ_b-independent Λ/g mass limit below which the combined constraints from Q_{weak} and APV rule out PV SL four-point contact interaction BSM physics. For the usual benchmark, $g^2 = 4\pi$, this flavor-independent mass limit is $\Lambda = 12.6$ TeV.

5.3. Constraints on Specific Extensions Beyond the Standard Model

Above, we have expressed the sensitivity of the Q_{weak} experiment to new BSM physics in terms of Λ/g in order to remain independent of the specific choice of coupling g associated with the New Physics. As mentioned above, however, it is conventional to compare the mass reach of different experiments (72) by using the specific coupling $g^2 = 4\pi$ (71) associated with compositeness (77). Compositeness posits that quarks and leptons have internal structure. Following this tradition, the Q_{weak} experiment has a mass reach $\Lambda = 26.6$ TeV (95% CL). The previous best SL ($eeqq$) mass reach for compositeness was 24 TeV (78), also at 95% CL.

However, $g^2 = 4\pi$ is on the high end of coupling strengths assumed for BSM physics. Perhaps a more natural size is $g \sim 1$, as is the case for the couplings of the known bosons. It could be even smaller. For example, a coupling strength of $g^2 = 4\pi\alpha$ is usually assumed for leptoquarks (79). Leptoquarks are theoretically postulated particles that have both lepton and baryon numbers and arise in SM extensions such as technicolor and Grand Unified Theories. The mass reach provided by the Q_{weak} result for leptoquarks (assuming $g^2 = 4\pi\alpha$) is only $\Lambda = 2.3$ TeV. This value still improves on the existing 95%-CL leptoquark mass reach of 1.755 TeV (80).

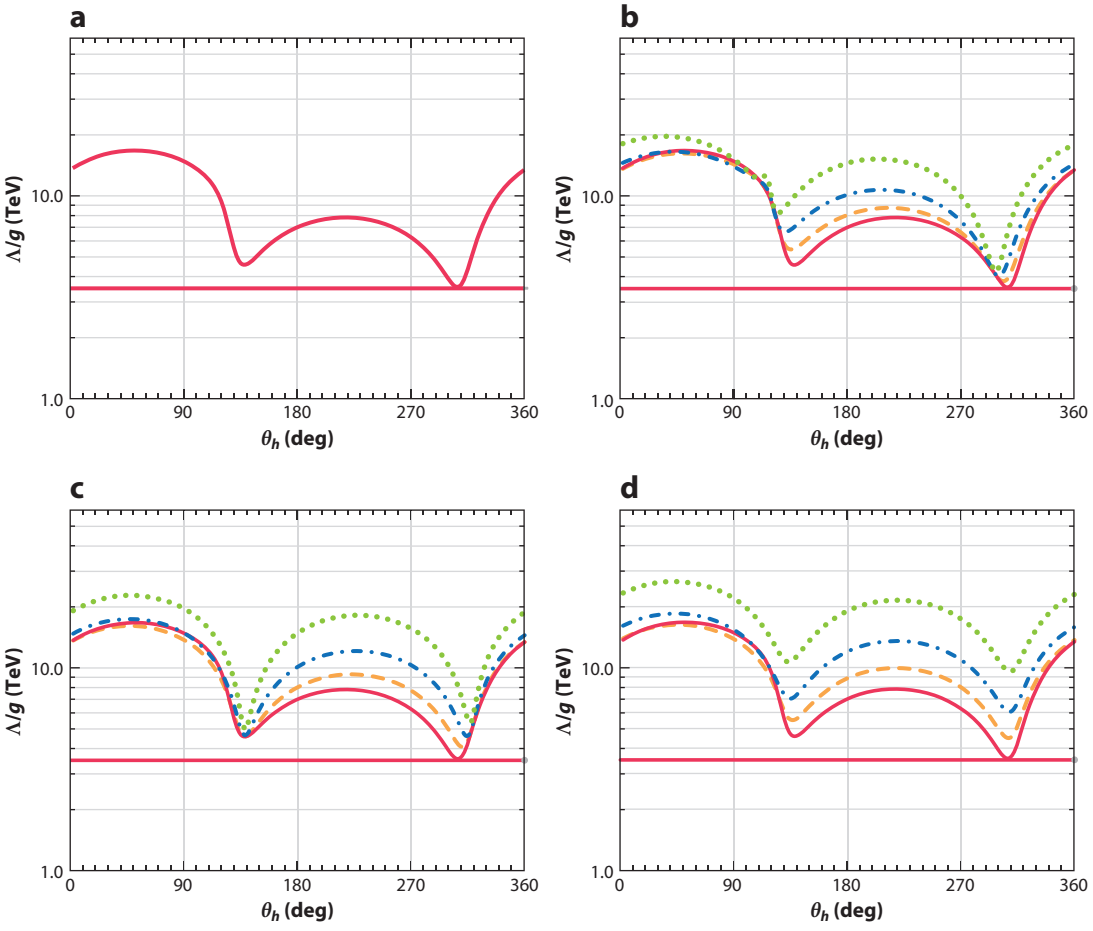

Figure 7

(*a*) A plot (*solid red curve*) of the mass reach Λ/g as a function of the flavor-mixing angle θ_b corresponding to the constraints provided by the Q_{weak} $\vec{e}p$ and cesium atomic parity-violation (APV) experiments. The horizontal red line denotes 3.5 TeV. (*b*) The three dashed curves denote what would happen with the addition of a future Q_W^p measurement with $\Delta Q_W^p = 0.0045$, 0.0045/2, or 0.0045/4. (*c*) The three dashed curves denote what would happen with the addition of a future APV measurement with ΔQ_W (cesium) =0.43, 0.43/2, or 0.43/4. (*d*) The three dashed curves represent what would happen with the addition of future Q_W^p and APV measurements, each with uncertainties equal to those available in the existing measurements, one-half the existing measurements, and one-quarter the existing measurements. Panel *a* adapted from Reference 8.

6. FUTURE PROSPECTS

There are two separate aspects to consider in order to evaluate the prospects of future experiments to measure the proton's weak charge: overcoming the experimental challenges and assessing the impact on the mass reach for BSM physics.

6.1. Experimental Challenges

The Q_{weak} result was statistics dominated: $A_{\text{ep}} = -226.5 \pm 7.3$ (stat.) $\pm$ 5.8 ppb (syst.). It required roughly 1 year of production running spread over 2 years. The first three of the Q_{weak} experiment's systematic uncertainties listed in **Table 1** made up two-thirds of the total systematic error. If the Q_{weak} experiment were to be repeated, it would certainly be feasible to reduce many of the

systematic uncertainties, but improving the total systematic uncertainty by more than a factor of two to three seems doubtful without significant changes to the kinematics, the apparatus, and the measured beam properties.

The P2 experiment (65), which aims to measure the proton's weak charge in a challenging experiment at a new facility (MESA) located in Mainz, Germany, differs significantly from the Q_{weak} experiment. The current P2 reference design (65) would employ 150 μA of 155 MeV longitudinally polarized electrons on a 60-cm-long liquid-hydrogen target at a mean angle of 35° and at a Q^2 of only 0.0045 GeV^2. The goals of the P2 experiment are to measure the expected −40 ppb asymmetry to 1.4% [±0.5 ppb (stat.) ±0.25 ppb (syst.)], the proton's weak charge to 1.5% (±0.0011), the weak mixing angle to 0.14% (±0.00033), and the mass reach Λ/g to 13.8 TeV (49 TeV with $g^2 = 4\pi$). The P2 strategy for achieving these ambitious goals is detailed in Reference 65.

The absolute statistical uncertainty achievable in the P2 experiment relative to that in the Q_{weak} experiment benefits from the higher *ep* elastic scattering cross section at their 5.5-times-lower Q^2, longer target, and larger solid-angle acceptance. As shown by Equation 5, the resulting smaller asymmetry reduces the FOM, but the trade-off with the smaller absolute statistical error results in a proposed fractional statistical uncertainty of 1.3%, which is a factor-of-2.3 improvement over Q_{weak}. Keeping the asymmetry statistical width close to the counting statistics limit will remain a challenge: Other random noise sources such as target noise, beam-current monitor width, detector resolution, and deadtimes from helicity switching and detector-signal processing must all be controlled better than they were in the Q_{weak} experiment.

The P2 requirements for the total fractional and absolute systematic uncertainty are, respectively, a factor of 4 and 23 more demanding than what Q_{weak} achieved. Systematic uncertainties associated with normalization factors such as beam polarization are similar to what Q_{weak} obtained. However, P2 cannot employ the Compton polarimetry technique due to the low beam energy, so it is developing a Møller polarimeter with trapped polarized-hydrogen atoms instead. Other systematic uncertainties, such as those from the beam-current monitors, the beamline background, the HCBAs, and some types of backgrounds, were among the largest contributions to the systematic uncertainty in the Q_{weak} experiment. The P2 goals for these represent a significant improvement over both the Q_{weak} fractional and the absolute systematic uncertainties. For example, differences in the relative beam charges measured in the three beam-current monitors used during the majority of the Q_{weak} experiment required the assignment of a 2.6 ppb systematic error.

6.2. Raising the Mass Reach for Physics Beyond the Standard Model

In this section, we focus on improvements to the mass reach for BSM physics that might be achieved in future experiments. The present limits and how they were arrived at are discussed in detail in Section 5. Those results include the mass reach on the proton set by the Q_{weak} experiment, as well as the flavor-independent mass reach provided by the combined results of the Q_{weak} experiment and the APV experiment on cesium. Here, we explore how each of these constraints might be improved with possible new experiments.

Making use of Equation 30 in Section 5, **Figure 8** shows how the 95%-CL mass reach on the proton depends on the uncertainty ΔQ_W^p attained in a measurement of Q_W^p. This figure assumes a central value for Q_W^p on the SM, as well as $\pm\Delta Q_W^p$ off the SM at each ΔQ_W^p. The P2 experiment's proposed goal of $\Delta Q_W^p = 0.0011$ is approximately four times better than the precision achieved in the Q_{weak} experiment, and thus nominally twice the mass reach achieved in the Q_{weak} experiment. Depending on where the P2 central value for Q_W^p falls within $\pm 1\sigma$ (i.e., ±0.0011) of the SM, the figure shows that the P2 mass reach Λ_+ (see Equation 30 with $g^2 = 4\pi$) could range anywhere

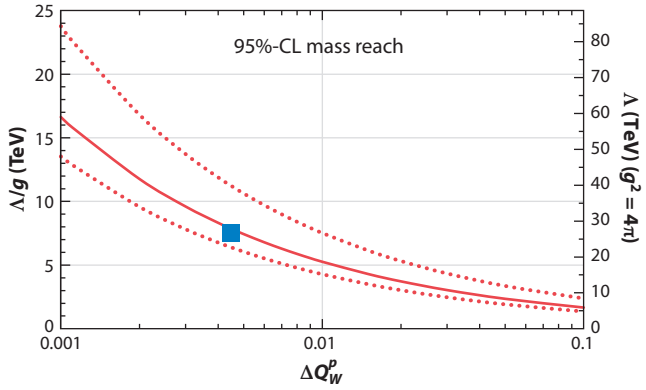

Figure 8

A plot of the 95%-CL mass reach Λ_+/g (and Λ_+ with $g^2 = 4\pi$; right axis) as a function of the uncertainty ΔQ_W^p in measurements of the proton's weak charge ($\theta_b = 26.6^\circ$) assuming a central value Q_W^p on the Standard Model (SM). The blue square denotes the existing constraint provided by the Q_{weak} experiment's result (8) with an uncertainty of ± 0.0045 and a central value of 0.0719, which is $+0.0008$ from the SM value. The dashed lines denote the boundaries defined by $\pm 1\sigma$ deviations of the assumed Q_W^p from the SM central value. Note that the uncertainty ΔQ_W^p proposed for the P2 experiment (65) is approximately 0.0011, which has the potential to deliver about twice the mass reach achieved in the Q_{weak} experiment.

from 46 to 80 TeV. This would constitute a significant improvement over the present limit of 26.6 TeV set by the Q_{weak} experiment.

Improving the flavor-independent mass reach is a much more difficult task because the present limit (Section 5.2) is already based on two precise experiments: the cesium APV result and the Q_{weak} result. **Figure 7*b*** depicts the likely discovery space for future Q_W^p experiments, **Figure 7*c*** shows the same for future APV experiments on cesium, and **Figure 7*d*** shows both. Each panel shows the existing 95%-CL Λ/g constraint as a function of the flavor-mixing angle θ_b, and then adds additional experiments with either the same uncertainty as or one-half/one-quarter the uncertainty of the existing experiments. The assumption is made that each new experiment's central value falls on the SM, and follows the same analysis procedure detailed in Section 5.2, except with the appropriate additional terms added to Equation 33. The resulting minimum Λ/g represents the mass limit below which PV SL four-point contact interaction BSM physics is excluded independently of what quark flavors the New Physics couples to. With a new Q_W^p measurement from P2 assuming a central value on the SM and assuming the ± 0.0011 uncertainty proposed for that experiment, combined with the existing Q_{weak} and APV cesium results, the θ_b-independent mass reach Λ/g would improve from 3.6 TeV to 4.2 TeV. The improvement in the θ_b-independent mass reach that could be achieved with new Q_W^p experiments, or with new APV experiments, is relatively modest compared with the improvement that could be achieved with both together.

7. SUMMARY

A solid foundation of expertise and knowledge acquired starting with the earliest PV experiments at LANL and SLAC, then later at TRIUMF, PSI, MIT-Bates, Mainz, and JLab, has made it possible to measure the PV *ep* asymmetry with the parts-per-billion-scale precision necessary to determine the proton's weak charge Q_W^p for the first time. These earlier experiments not only incrementally taught the PV community how to do these challenging measurements but also provided the hadronic structure information needed to extract the weak charge from

the precise Q_{weak} experiment's asymmetry measurement ($A_{ep} = -226.5 \pm 9.3$ ppb) targeted near threshold at $Q^2 = 0.00248$ GeV^2. The result of this decades-long effort was a 6.3% measure of $Q_W^p = 0.0719 \pm 0.0045$, which is in close agreement with the SM value, $Q_W^p = 0.0711 \pm 0.0002$.

This article has described some of the most relevant aspects of this Q_{weak} experiment. We have explained in detail how consistent results for the proton's weak charge are extracted using several different methods employing varying degrees of input from data and calculated form factors. The resulting Q_W^p has been used to determine the most precise measure of the weak mixing angle below the Z pole, $\sin^2\theta_W(Q = 0.158\ \text{GeV}) = 0.2382 \pm 0.0111$, and compared with determinations from other experiments. We have described the $\Lambda/g = 7.5$ TeV mass reach determined at 95% CL from the Q_{weak} result for BSM physics on the proton, as well as for any combination of quark flavors by including the APV result on cesium: $\Lambda/g = 3.6$ TeV. With the usual $g^2 = 4\pi$ associated with compositeness and commonly used for comparisons with other experiments, these mass limits correspond to $\Lambda = 26.6$ TeV and $\Lambda = 12.6$ TeV, respectively. Finally, we have explored the impact new experiments could have on these mass limits. The community looks forward to a bright future with the next generation of experiments.

DISCLOSURE STATEMENT

The authors are not aware of any affiliations, memberships, funding, or financial holdings that might be perceived as affecting the objectivity of this review.

ACKNOWLEDGMENTS

The authors thank all their collaborators on the Q_{weak} experiment, as well as the staffs of JLab, TRIUMF, and the MIT-Bates laboratory. The writing of this review was supported by the US Department of Energy (DOE), contract DEAC05-06OR23177, under which Jefferson Science Associates, LLC, operates the Thomas Jefferson National Accelerator Facility. Construction and operating funding for the Q_{weak} experiment was provided through the DOE, the Natural Sciences and Engineering Research Council of Canada, the Canadian Foundation for Innovation, and the National Science Foundation with matching contributions from the College of William and Mary, Virginia Tech, George Washington University, and Louisiana Tech University.

LITERATURE CITED

1. Aad G, et al. (ATLAS Collab.). *Phys. Lett. B* 716:1 (2012)
2. Chatrchyan S, et al. (CMS Collab.). *Phys. Lett. B* 716:30 (2012)
3. Erler J, Su S. *Prog. Part. Nucl. Phys.* 71:119 (2013)
4. Erler J, et al. *Annu. Rev. Nucl. Part. Sci.* 64:269 (2014)
5. Potter JM, et al. *Phys. Rev. Lett.* 33:1307 (1974)
6. Prescott CY, et al. *Phys. Lett. B* 84:524 (1979)
7. Anthony PL, et al. *Phys. Rev. Lett.* 95:08161 (2005)
8. Androić D, et al. (Qweak Collab.). *Nature* 557:207 (2018)
9. Allison T, et al. (Qweak Collab.). *Nucl. Instrum. Methods A* 781:105 (2015)
10. Duvall WS. *Precision measurement of the proton's weak charge using parity-violating electron scattering*. PhD thesis, Va. Polytech. Inst. State Univ., Blacksburg (2017)
11. Myers KE. *The first determination of the proton's weak charge through parity-violating asymmetry measurements in elastic* e + p *and* e + *Al scattering*. PhD thesis, George Wash. Univ., Washington, DC (2012)
12. Magee JA. *A measurement of the parity-violating asymmetry in aluminum and its contribution to a measurement of the proton's weak charge*. PhD thesis, Coll. William Mary, Williamsburg, VA (2016)

13. Bartlett KD. *First measurements of the parity-violating and beam-normal single-spin asymmetries in elastic electron–aluminum scattering*. PhD thesis, Coll. William Mary, Williamsburg, VA (2018)
14. Kargiantoulakis E. *A precision test of the standard model via parity-violating electron scattering in the Qweak experiment*. PhD thesis, Univ. Va., Charlottesville (2015)
15. Jones DC. *Measuring the weak charge of the proton via elastic electron–proton scattering*. PhD thesis, Univ. Va., Charlottesville (2015)
16. Gray VM. *Determination of the kinematics of the Qweak experiment and investigation of an atomic hydrogen Møller polarimeter*. PhD thesis, Coll. William Mary, Williamsburg, VA (2018)
17. Hauger M, et al. *Nucl. Instrum. Methods A* 462:382 (2001)
18. Narayan A, et al. *Phys. Rev. X* 6:011013 (2016)
19. Ito TM, et al. (SAMPLE Collab.). *Phys. Rev. Lett.* 92:102003 (2004)
20. Spayde DT, et al. (SAMPLE Collab.). *Phys. Lett. B* 583:79 (2004)
21. Maas FE, et al. (PVA4 Collab.). *Phys. Rev. Lett.* 93:022002 (2004)
22. Maas FE, et al. (PVA4 Collab.). *Phys. Rev. Lett.* 94:152001 (2005)
23. Baunack S, et al. (PVA4 Collab.). *Phys. Rev. Lett.* 102:151803 (2009)
24. Balaguer Ríos D, et al. *Phys. Rev. D* 94:051101 (2016)
25. Armstrong DS, et al. (G0 Collab.). *Phys. Rev. Lett.* 95:092001 (2005)
26. Androić D, et al. (G0 Collab.). *Phys. Rev. Lett.* 104:012001 (2010)
27. Aniol KA, et al. (HAPPEX Collab.). *Phys. Rev. C* 69:065501 (2004)
28. Aniol KA, et al. (HAPPEX Collab.). *Phys. Lett. B* 635:275 (2006)
29. Aniol KA, et al. (HAPPEX Collab.). *Phys. Rev. Lett.* 96:022003 (2006)
30. Acha A, et al. (HAPPEX Collab.). *Phys. Rev. Lett.* 98:032301 (2007)
31. Ahmed Z, et al. (HAPPEX Collab.). *Phys. Rev. Lett.* 108:102001 (2012)
32. Androić D, et al. (Qweak Collab.). *Phys. Rev. Lett.* 111:141803 (2013)
33. Arrington J, Sick I. *Phys. Rev. C* 76:035201 (2007)
34. Zhu SL, Puglia SJ, Holstein BR, Ramsey-Musolf MJ. *Phys. Rev. D* 62:033008 (2000)
35. Tanabashi M, et al. (Part. Data Group). *Phys. Rev. D* 98:030001 (2018)
36. Hall NL, et al. *Phys. Lett. B* 753:221 (2016)
37. Blunden PG, Melnitchouk W, Thomas AW. *Phys. Rev. Lett.* 107:081801 (2011)
38. Blunden PG, Melnitchouk W, Thomas AW. *Phys. Rev. Lett.* 109:262301 (2012)
39. Gorchtein M, Horowitz CJ, Ramsey-Musolf MJ. *Phys. Rev. C* 84:015502 (2011)
40. Gorchtein M, Spiesberger H, Zhang X. *Phys. Lett. B* 752:135 (2016)
41. Rislow BC, Carlson CE. *Phys. Rev. D* 83:113007 (2011)
42. Hall NL, et al. (AJM Collab.). *Phys. Rev. D* 88:013011 (2013)
43. Hall NL, et al. (AJM Collab.). *Phys. Lett. B* 753:221 (2016)
44. Gorchtein M, Horowitz CJ, Ramsey-Musolf MJ. *Phys. Rev. C* 84:015502 (2011)
45. Green J, et al. *Phys. Rev. D* 92:031501 (2015)
46. Sufian RS, et al. *Phys. Rev. Lett.* 118:042001 (2017)
47. Young RD, Roche J, Carlini RD, Thomas AW. *Phys. Rev. Lett.* 97:102002 (2006)
48. Liu J, McKeown RD, Ramsey-Musolf MJ. *Phys. Rev. C* 76:025202 (2007)
49. Higinbotham DW, et al. *Phys. Rev. C* 93:055207 (2016)
50. Griffioen K, Carlson C, Maddox S. *Phys. Rev. C* 93:065207 (2016)
51. Zhan X, et al. *Phys. Lett. B* 705:59 (2011)
52. Antognini A, et al. *Science* 339:417 (2013)
53. Kelly JJ. *Phys. Rev. C* 70:068202 (2004)
54. Galster S, et al. *Nucl. Phys. B* 32:221 (1971)
55. Venkat S, Arrington J, Miller GA, Zhan X. *Phys. Rev. C* 83:015203 (2011)
56. Erler J, Ramsey-Musolf MJ. *Phys. Rev. D* 72:073003 (2005)
57. Erler J, Ferro-Hernández R. *J. High Energy Phys.* 1803:196 (2018)
58. Patrignani C, et al. (Part. Data Group). *Chin. Phys. C* 40:100001 (2016)
59. Ramsey-Musolf MJ. *Phys. Rev. C* 60:015501 (1999)
60. Wood CS, et al. *Science* 275:1759 (1997)

61. Dzuba VA, Berengut JC, Flambaum VV, Roberts B. *Phys. Rev. Lett.* 109:203003 (2012)
62. Zeller GP, et al. (NuTeV Collab.). *Phys. Rev. Lett.* 88:091802 (2002)
63. Bentz W, Cloët IC, Londergan JT, Thomas AW. *Phys. Lett. B* 693:462 (2010)
64. Langacker P. *Nucl. Phys. B Proc. Suppl.* 38:152 (1995)
65. Becker D, et al. *Eur. Phys. J. A* 54:208 (2018)
66. Benesch J, et al. arXiv:1411.4088 [nucl-ex] (2014)
67. Jefferson Lab PVDIS Collab. *Nature* 506:67 (2014)
68. Chen JP, et al. arXiv:1409:7741 [nucl-ex] (2014)
69. Zhao YX, et al. arXiv:1701:02780 [nucl-ex] (2017)
70. Young RD, Carlini RD, Thomas AW, Roche J. *Phys. Rev. Lett.* 99:122003 (2007)
71. Eichten E, Lane KD, Peskin ME. *Phys. Rev. Lett.* 50:811 (1983)
72. Erler J, Horowitz CJ, Mantry S, Souder PA. *Annu. Rev. Nucl. Part. Sci.* 64:269 (2014)
73. Bennett SC, Wieman CE. *Phys. Rev. Lett.* 82:2484 (1999)
74. Edwards NH, et al. *Phys. Rev. Lett.* 74:2654 (1995)
75. MacPherson MJD, et al. *Phys. Rev. Lett.* 67:2784 (1991)
76. Meekhof DM, et al. *Phys. Rev. Lett.* 71:3442 (1993)
77. Hikasa K, et al. (Part. Data Group). 112. Searches for quarks and lepton compositeness. See Ref. 35. **http://pdg.lbl.gov/2018/reviews/rpp2018-rev-searches-quark-lep-compositeness.pdf** (2018)
78. Tanabashi M, et al. (Part. Data Group). PDGLive: Searches for quark and lepton compositeness. See Ref. 35. **http://pdglive.lbl.gov/Particle.action?node=S054** (2018)
79. Rolli S, et al. (Part. Data Group). 115. Leptoquarks. See Ref. 35. **http://pdg.lbl.gov/2018/reviews/rpp2018-rev-leptoquark-quantum-numbers.pdf** (2018)
80. Tanabashi M, et al. (Part. Data Group). PDGLive: Searches for new heavy bosons (W', Z', leptoquarks, etc.). See Ref. 35. **http://pdglive.lbl.gov/Particle.action?node=S056** (2018)

Annual Review of Nuclear and Particle Science

Volume 69, 2019

Contents

Errata

An online log of corrections to *Annual Review of Nuclear and Particle Science* articles may be found at http://www.annualreviews.org/errata/nucl